Fuel 416 (2026) 138472

Contents lists available at ScienceDirect

Fuel

journal homepage: www.elsevier.com/locate/jfue

Full length article

Computational study on the pyrolysis of 2,5-diketopiperazine: From electronic structure calculations to kinetic modeling

Bastian Schnieder[a,*], Paulo Debiagi[b], Matteo Pelucchi[c], Rochus Schmid[d], Christof Hättig[a]

[a] Ruhr-Universität Bochum, Lehrstuhl für Theoretische Chemie I, 44780 Bochum, Germany
[b] University of Nottingham Ningbo China, Nottingham Ningbo China Beacons of Excellence Research and Innovation Institute, Ningbo, China
[c] Department of Chemistry, Materials and Chemical Engineering "G. Natta", Politecnico di Milano, Milan, Italy
[d] Ruhr-Universität Bochum, Lehrstuhl Anorganische Chemie 2, Computational Materials Chemistry group, 44780 Bochum, Germany

HIGHLIGHTS

- An automated workflow combines MD and electronic structure calculations to build a kinetic model for pyrolysis.
- The model, implemented in OpenSMOKE++, reproduces qualitatively experimental DKP pyrolysis products in the kinetic regime.
- Ammonia is not formed during primary decomposition but through secondary reactions.

GRAPHICAL ABSTRACT

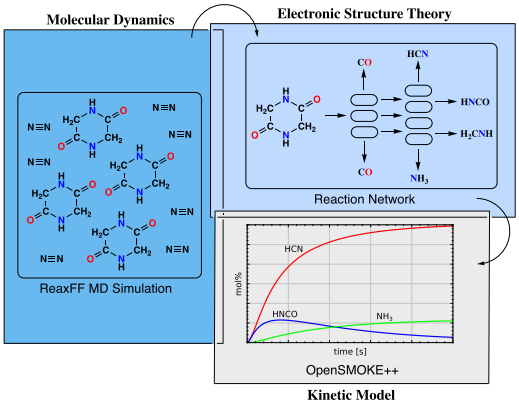

ARTICLE INFO

Keywords:
Biomass
Pyrolysis
Diketopiperazine
DFT
NO_X
Kinetic modeling

ABSTRACT

Pyrolysis is an important thermochemical conversion process for biomass and is conducted in the absence of oxygen at temperatures between 400 and 1000 °C. Biomass pyrolysis yields cleaner combustion fuels by decreasing fuel-bound oxygen and nitrogen species, thus reducing NO_X formation and net CO_2 emissions. A structural model compound for cyclic peptides — important nitrogen-containing components in biomass — is 2,5-diketopiperazine (DKP). In this work, we apply an automated workflow that combines reactive molecular dynamics simulations with electronic structure calculations at different levels of theory to develop a detailed kinetic model for the pyrolysis of DKP at the level of elementary reaction steps. This complements previous studies that focused only on the net reaction scheme. The developed DKP kinetic submodel for pyrolysis is implemented in the kinetic modeling software `OpenSMOKE++`. Under pyrolysis, DKP decomposes into hydrogen cyanide (HCN), carbon monoxide (CO) and hydrogen (H_2). Ammonia (NH_3) is not formed in primary decomposition steps but rather in secondary reactions involving the primary intermediates. The submodel qualitatively reproduces DKP pyrolysis products observed in a fluidized bed reactor under kinetically controlled conditions and provides a reliable basis for further studies on peptide decomposition. Beyond the specific kinetic submodel, this work proposes a general workflow for investigating thermal decomposition and combustion processes.

* Corresponding author.
Email address: bastian.schnieder@ruhr-uni-bochum.de (B. Schnieder).

https://doi.org/10.1016/j.fuel.2026.138472
Received 3 September 2025; Received in revised form 12 January 2026; Accepted 18 January 2026
Available online 25 January 2026

1. Introduction

Over the past two decades, the transition from fossil-fuel-based energy production to renewable and sustainable alternatives has highlighted biomass as a key baseload for heat and power generation [1]. The calorific value of biomass lies in the range of 14-30 MJ/kg, comparable to coal-based fuels (25-35 MJ/kg) [2]. Direct combustion of biomass and biochar can be used for electricity generation and represents a renewable alternative to coal and lignite combustion [3]. However, instead of relying on direct combustion, biomass can also be converted through pyrolysis into valuable industrial products such as char, bio-oil, and gases [4]. Among the thermochemical conversion processes, pyrolysis is not only the most widespread one but also forms the basis of oxidation (combustion) or partial oxidation and reforming (gasification) processes. Pyrolysis takes place in heated reactors in the absence of oxygen, typically at temperatures between 400 and 1000 °C [5].

Modeling these chemical conversion processes, both atomistically and macroscopically, is particularly complex, because the physical or chemical properties depend on the biomass feedstock and the reaction products in addition to operating temperature, contact times, heating rates, and particle size [6–8]. The devolatilization of the solid particles releases condensable and uncondensable fragments into the gas phase along with the formation of a solid char residue [9]. During the pyrolytic conversion of nitrogen-rich biomass, fuel-nitrogen is converted and released into the gas phase as a variety of N-containing compounds. In oxidation environments, these compounds are precursors to NO_X formation [10–13]. Among the N-containing compounds, 2,5-diketopiperazine (DKP) is an important product that can originate from the dehydration of the amino acid glycine during biomass conversion (Fig. 1) [14,15]. Experimental studies have shown that the main pyrolysis products of DKP include hydrogen cyanide (HCN), isocyanic acid (HNCO), carbon monoxide (CO), and ammonia (NH_3) [16,17]. Oxidation of such NO_X precursors—whether in reactors (e.g., combustors or gasifiers) or in the atmosphere—produces nitrogen oxides (NO_X) [18] that have a negative impact on human health and ecosystems [19–21]. Numerous studies have explored the conversion pathways of NO_X precursors to actual NO_X gases (NO and NO_2) and made them available in various kinetic models [22–30].

The pyrolysis and combustion processes of DKP are only partly understood at the atomistic level. Previous research focused primarily on experimental studies of direct DKP conversion into a variety of products without elucidating the underlying mechanisms and dynamics of radical intermediates [17,31]. Understanding the formation pathways of NO_X precursors is crucial for optimizing biomass conversion and for emission control strategies.

The aim of the current study is to theoretically unravel DKP pyrolysis mechanisms and to propose a detailed kinetic submodel capable of qualitatively predicting the yield and rate of formation of pyrolysis products, including NO_X precursors. The developed submodel is coupled to the `CRECK` kinetic framework [32,33] for nitrogen-containing fuels and is provided in `CHEMKIN` format for integration into other existing kinetic models.

In recent years, Yönder et al. [34] and Schnieder et al. [35] have contributed to a more detailed understanding of the evolution of oxygen and sulfur functional groups during the thermochemical conversion of biochar. The present study extends this work to fuel-nitrogen species originating from DKP as a model compound for peptide-based molecules. We employ molecular dynamics (MD) simulations with the reactive force field ReaxFF [36,37] to explore pyrolytic conversion pathways. The MD trajectories were analyzed using an automated workflow developed by Schmitz et al. [38], identifying reaction events that are subsequently refined using first-principles electronic structure calculations. In addition to molecular reaction mechanisms, we report temperature-dependent thermodynamic and kinetic parameters, including thermodynamic properties provided in the `NASA-7` polynomial format [39] and kinetic rate constants in the form of modified Arrhenius equations. To evaluate the predictive capability of the DKP submodel, the kinetic modeling software `OpenSMOKE++` has been used to simulate the evolution of NO_X precursors during pyrolysis in both batch and plug flow reactors (PFR). The predicted concentrations of different NO_X precursors are compared with experimental results obtained in a real PFR setup.

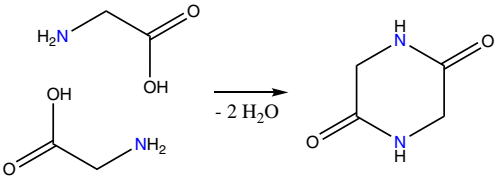

Fig. 1. 2,5-Diketopiperazine (DKP) formed as the condensation product of two glycine amino acids ($C_2H_5NO_2$).

2. Methods

2.1. Molecular dynamics simulations

The pyrolysis of 2,5-diketopiperazine (DKP) was simulated in a nitrogen atmosphere using molecular dynamics (MD) simulations with the reactive force field ReaxFF [36,37]. The `CHOSFClN` parametrization [40], specifically parameterized for the thermal decomposition of organic compounds was employed. The ReaxFF simulations were performed using our in-house `Python` interface to the Molecular Dynamics Simulator `LAMMPS` [41].

The cubic simulation box was packed with 100 DKP and 500 N_2 molecules with a density of 0.66 mg/cm^3. The system was equilibrated for 50 fs before the simulations at a temperature of 2000 K (time step $\tau = 0.1$ fs) using the Nosé-Hoover thermostat. A total of three trajectories was generated using different randomly assigned initial velocities. To analyze the ReaxFF concentration profiles, one trajectory was simulated until DKP conversion reached 100% (at 13.6 ns) and was used for further analysis. The simulations were performed in the canonical ensemble and applied periodic boundary conditions. Tracking of key NO_x precursors, pyrolysis products as well as of C_1-C_4 species was realized by the graph-based `findR` [42] program. The ReaxFF concentration profiles presented in Section 3.1 were smoothed using the Savitzky-Golay filter [43] implemented in the `SciPy` [44] library for `Python`.

2.2. Electronic structure calculations

Reaction events identified in the ReaxFF trajectories were refined with electronic structure calculations using the automated workflow described in Ref. [38]. The focus was on pyrolysis reactions of DKP that lead to the release of NO_X precursors. All electronic structure calculations were performed with the `TURBOMOLE` program package [45] version 7.6. We employed the resolution of identity (RI-J) approximation [46] for the Coulomb potential with optimized auxiliary basis sets [47] and Grimme's D3 dispersion correction [48]. Initial structures from the MD simulation were optimized using Density Functional Theory (DFT) with the TPSS meta-GGA functional [49] and the def-SVP basis set [50]. Final geometries and vibrational frequencies were computed using the TPSSh meta-hybrid functional [51] and the def-TZVP basis set [52]. For the DFT calculations we employed the `ridft` and `rdgrad` modules of `TURBOMOLE`. Zero-point vibrational (ZPV) energies were scaled by a factor of 0.9874 for the TPSSh functional taken from Ref. [53] and added to the electronic energy. Electronic reaction energies (E_{rxn}) and activation barriers (E_{act}) were calculated according to:

$$E_{rxn} = \sum_{i}^{products} (E_{el,i} + E_{ZPV,i}) - \sum_{i}^{reactants} (E_{el,i} + E_{ZPV,i}) \quad (1)$$

$$E_{act} = E_{el,TS} + E_{ZPV,TS} - \sum_{i}^{reactants} (E_{el,i} + E_{ZPV,i}) \quad (2)$$

Above, $E_{ZPV,i}$ is the ZPV energy of molecular species i with an electronic energy $E_{el,i}$. The electronic energy of the transition state is denoted with $E_{el,TS}$. While DFT geometries and vibrational energies are sufficiently accurate for the purpose of this project, the electronic energies were further improved with single-point calculations at the level of explicitly correlated coupled cluster singles and doubles with a perturbative correction for connected triples [54], CCSD(F12*)(T*). All coupled cluster (CC) calculations were done with TURBOMOLE's `ccsdf12` program and used the frozen-core approximation applied to the $1s^2$ cores of carbon, nitrogen, and oxygen and the cc-pVDZ-F12 orbital [55], auxiliary [56,57], and complementary auxiliary basis sets [58]. For the CC calculations restricted (open-shell) Hartree-Fock reference wavefunctions were used. The latter were computed with the `dscf` module [59]. Reaction pathways were obtained with the chain-of-state method [60–62] implemented in the `woelfling` program. The transition states were then optimized with the trust-region image minimization algorithm [63] (module `statpt`) and validated by intrinsic reaction coordinate calculations (module `DRC`).

Rate constants k were computed for reactions with significant activation barriers as in Ref. [64] using classical transition state theory with the ideal gas law as the equation of state at isobaric conditions (1 atm):

$$k(T) = \kappa \frac{k_b T}{h} \frac{Q_{TS}/V}{\Pi_{i=educts}(Q_i/V)} \exp\left(-\frac{E_{el,act}}{RT}\right). \quad (3)$$

In the last equation, Q_{TS} denotes the partition function of the transition state and Q_i that of molecular species i. V is the volume per particle in the translational partition function, $Q_{trans}/V = (2\pi k_b T m/h^2)^{3/2}$ for a particle with mass m. Furthermore, R is the ideal gas constant, T the absolute temperature, h the Planck constant, k_b the Boltzmann constant, and $E_{el,act}$ the electronic activation energy at the transition state. Partition functions were obtained by applying a modified rigid rotor harmonic oscillator approximation (qRRHO) [65,66]. The transmission coefficient κ is calculated within the high-temperature limit of the Eckart tunneling correction [67]. Let υ be the imaginary frequency of the transition state, then κ is defined within this approximation as

$$\kappa = 1 - \frac{1}{24}\left(\frac{h\upsilon}{k_b T}\right)^2 \left(1 + \frac{RT}{E_{el,act}}\right). \quad (4)$$

We provide high-pressure limit rate constants calculated on a grid (271 points) for the temperature range of 300 to 3000 K. To interpolate between the computed points, modified Arrhenius expressions (Eq. 5) were fitted to them using a nonlinear least-squares fit.

$$\mathrm{k} = A T^n \exp\left(-\frac{E}{T}\right) \quad (5)$$

2.3. Thermodynamic properties

For the implementation of the newly discovered reaction pathways in `OpenSMOKE++` [68], the thermodynamic properties of molecular species that were not yet included in the available parameter sets were calculated from the partition functions computed as described above. For each species the isobaric heat capacity C_p, enthalpy ΔH, and entropy ΔS (at 1 bar) were fitted to `NASA-7` polynomials as proposed by Gordon and McBride [69] in the temperature range from 200 to 5000 K. Enthalpies and entropies were fitted with respect to the heat and entropy of formation so that, under standard conditions, the computed values of ΔH and ΔS reproduce the standard enthalpy and entropy of formation. Details for the calculation of ΔH_f° and ΔS_f° for species not included in the `NIST` database are provided in the Supplementary Information. The fitting procedure adapted from Ref. [70] was implemented in a `Python` function (available in Ref. [71]) in the workflow following the methodology described in the original publication [69]. A nonlinear least-squares fit is performed iteratively thereby testing different cut-off temperatures in 10 K intervals and using the one with the lowest residual. During the fitting process, the heat capacity coefficients a_1-a_5 are fitted first. Then, the enthalpy coefficient a_6 is adjusted with fixed C_p coefficients. Lastly, a_7 is fitted to match the entropy data. The only deviation from the original implementation is the omission of explicitly enforcing continuity between the high- and low-temperature limits, as `OpenSMOKE++` automatically corrects any such discontinuities in the thermodynamic properties [68]. Additionally, calculated rate expressions reported in Table 3 together with the `NASA-7` polynomials were incorporated into the kinetic modeling software `OpenSMOKE++`.

2.4. Kinetic modeling

The kinetic modeling software `OpenSMOKE++` (version 22.0) [68,72,73] was used to perform ideal batch reactor and plug flow reactor simulations. The ideal batch reactor was simulated at isothermal conditions with constant volume. The initial reactor conditions were set to 1/6 mol% DKP in an N_2 atmosphere at $p = 1$ bar. The new DKP submodel was added to the `CRECK 2003 TOT HT LT SOOT NOX` [32,33] mechanism. Temperature and reaction duration were varied between, respectively, 1000–2000 K and 0.0–1.0 s to obtain concentration profiles of the main pyrolysis products. The sum of the concentrations (mol%)

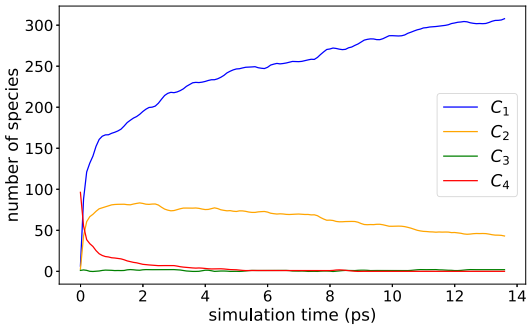

(a) C_1-C_4 compounds.

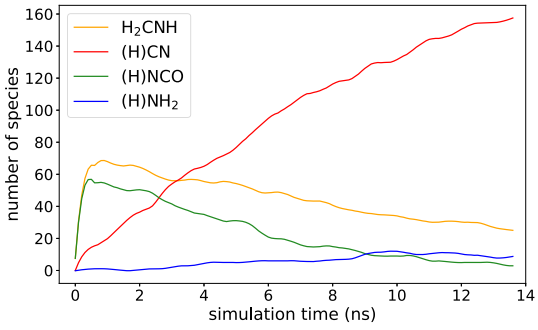

(b) NO_X precursors.

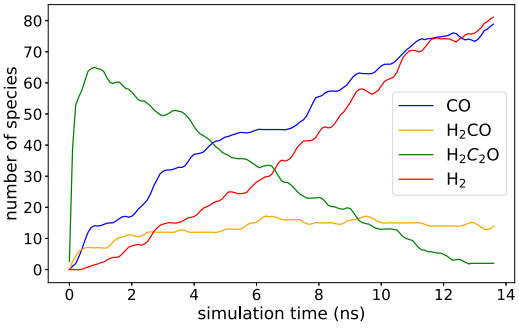

(c) $(H_y)CO_x$ compounds.

Fig. 2. Time evolution of important molecular species formed during the ReaxFF simulation of the pyrolysis of 2,5-diketopiperazine.

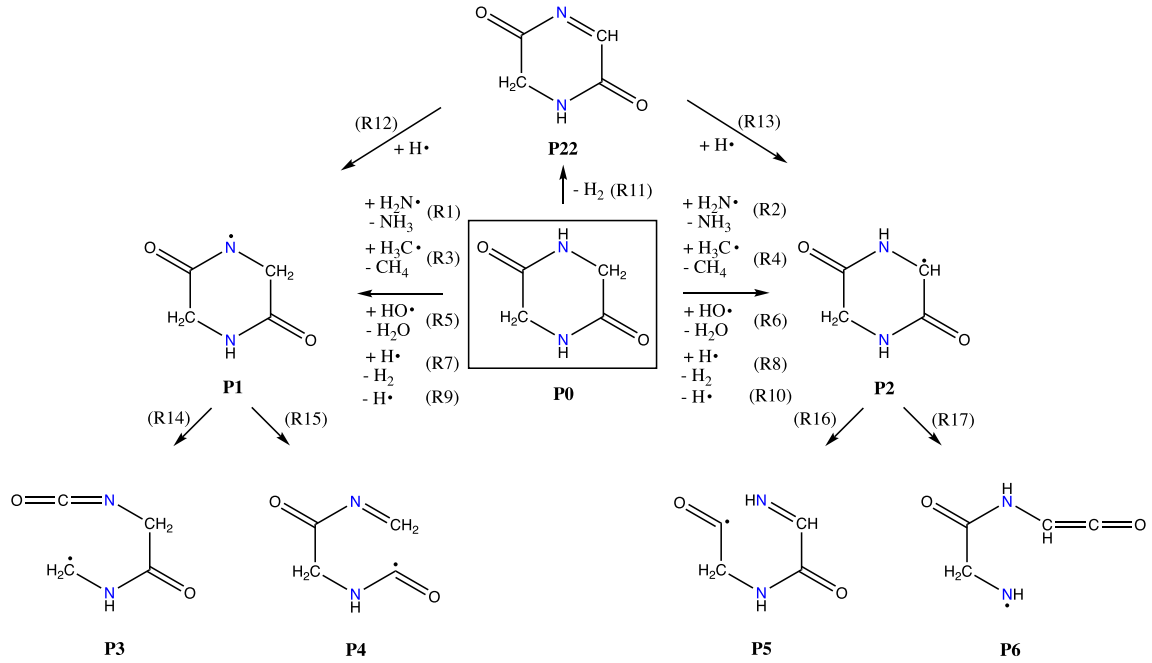

Fig. 3. Comparison of different initiation reactions of 2,5-Diketopiperazine (**P0**) leading to the acyclic intermediates **P3** – **P6**.

Table 1
DFT TPSSh-D3/TZVP and CCSD(F12*)(T*)/cc-pVDZ-F12 Energies for Initiation Pathways of 2,5-Diketopiperazine (Fig. 3) in kJ/mol.

Reaction	$E_{act,DFT}$	$E_{rxn,DFT}$	$E_{act,CC}$	$E_{rxn,CC}$
(R1) P0 + H_2N → P1 + NH_3	barrierless	−1.1	44.1	7.5
(R2) P0 + H_2N → P2 + NH_3	barrierless	−87.8	18.5	−88.7
(R3) P0 + H_3C → P1 + CH_4	34.6	0.2	61.1	17.7
(R4) P0 + H_3C → P2 + CH_4	13.4	−86.5	32.6	−78.5
(R5) P0 + HO → P1 + H_2O	barrierless	−41.2	–	−41.8
(R6) P0 + HO → P2 + H_2O	barrierless	−127.9	–	−138.0
(R7) P0 + H → P1 + H_2	21.5	−18.7	72.1	17.6
(R8) P0 + H → P2 + H_2	barrierless	−105.4	21.8	−78.6
(R9) P0 → P1 + H	barrierless	425.9	–	447.7
(R10) P0 → P2 + H	barrierless	339.2	–	351.5
(R11) P0 → P22 + H_2	417.1	152.1	316.6	150.5
(R12) P22 + H → P1	barrierless	−170.8	–	−132.8
(R13) P22 + H → P2	barrierless	−257.5	–	−229.0
(R14) P1 → P3	32.0	−11.5	39.9	−9.3
(R15) P1 → P4	87.7	67.9	88.4	56.7
(R16) P2 → P5	172.9	162.9	177.2	149.6
(R17) P2 → P6	barrierless	222.9	–	225.4

Table 2
DFT TPSSh-D3/TZVP and CCSD(F12*)(T*)/cc-pVDZ-F12 Energies for Initiation Pathways of 2,5-Diketopiperazine in kJ/mol.

Reaction	$E_{act,DFT}$	$E_{rxn,DFT}$	$E_{act,CC}$	$E_{rxn,CC}$
P3 → P7 + P8	barrierless	141.5	–	126.4
P8 → P9 + P10	barrierless	109.2	–	118.1
P4 → P11 + P12	54.3	3.6	81.2	5.9
P12 → P9 + P13	105.4	72.6	126.5	78.1
P4 → P14 + CO	96.1	89.9	91.3	64.7
P14 → P7 + P15	barrierless	−19.9	–	−6.4
P15 → P13 + CO	118.1	90.6	99.8	47.5
P5 → P9 + P16	barrierless	125.8	–	143.1
P16 → P11 + P21	46.6	0.9	59.3	−4.1
P5 → P17 + CO	22.7	6.1	35.0	0.6
P17 → P7 + P18	barrierless	157.5	–	134.0
P18 → P21 + CO	54.4	47.4	53.0	26.3
P6 → P7 + P19	76.8	71.8	90.5	68.4
P19 → P11 + P20	49.4	24.9	77.7	28.5

of the main products (HCN, NH_3, CO, H_2, H_2CNH, and HNCO) were scaled to sum up to 100%. All concentration profiles were interpolated between the computed points using the PCHIP shape-preserving interpolator [44]. Analogously, the plug flow reactor (PFR) was simulated with a residence time of 10 s, corresponding to a reactor length of 10.5 m and a gas flow velocity of 1.0 m/s. An initial concentration of 1 mol% DKP was used in the PFR. To compare the PFR products to the experimental results for NO_X fractions reported by Hansson et al. [15], the simulated mass fractions of HCN, NH_3, and HNCO were scaled to 100%. For barrierless reactions, the activation barrier of the reverse reaction is set equal to the reaction energy, and a pre-exponential factor of 10^{13} s^{-1} is used.

3. Results and discussion

3.1. Atomistic pyrolysis simulation

In the first stage of this study, the pyrolysis of DKP was analyzed by examining the longest ReaxFF MD trajectory for the main decomposition products. The number of species containing different numbers of carbon atoms (C_1-C_4), CO_X species, and NO_X precursors were monitored as a function of simulation time (Fig. 2). At elevated temperatures (2000 K), the decomposition of DKP began immediately, forming C_1 intermediates. The amount of C_1 products increased continuously over time, while the formation of C_2 compounds (mostly ketenes) declined after an induction period of 1 ns. The formation of C_3 occurred only rarely, as they were only generated by the addition of C_1 and C_2 fragments. After 5 ns, over 90% of the DKP was decomposed into smaller species.

Further analysis (Figs. 2(b) and 2(c)) indicates that the initial elimination products are primarily methylene imine (H_2CNH), isocyanic acid (HNCO), and ethenone (H_2CCO). At around 0.5 ns the amount of methylene imine surpassed that of isocyanic acid. After approximately 0.8 ns the concentrations of these three initial products began to decline. Methylene imine and isocyanic acid were converted into cyanides (HCN, CN), while ethenone decomposed to carbon monoxide (CO) and hydrogen (H_2). The concentration of cyanides exceeded that of HNCO after 2 ns, and surpassed H_2CNH after 3 ns.

The main pyrolysis products predicted by ReaxFF after 13.6 ns are CO, HCN, and H_2. The results of the ReaxFF simulation agree qualitatively with the experimental observations of Liu et al. [17] who report

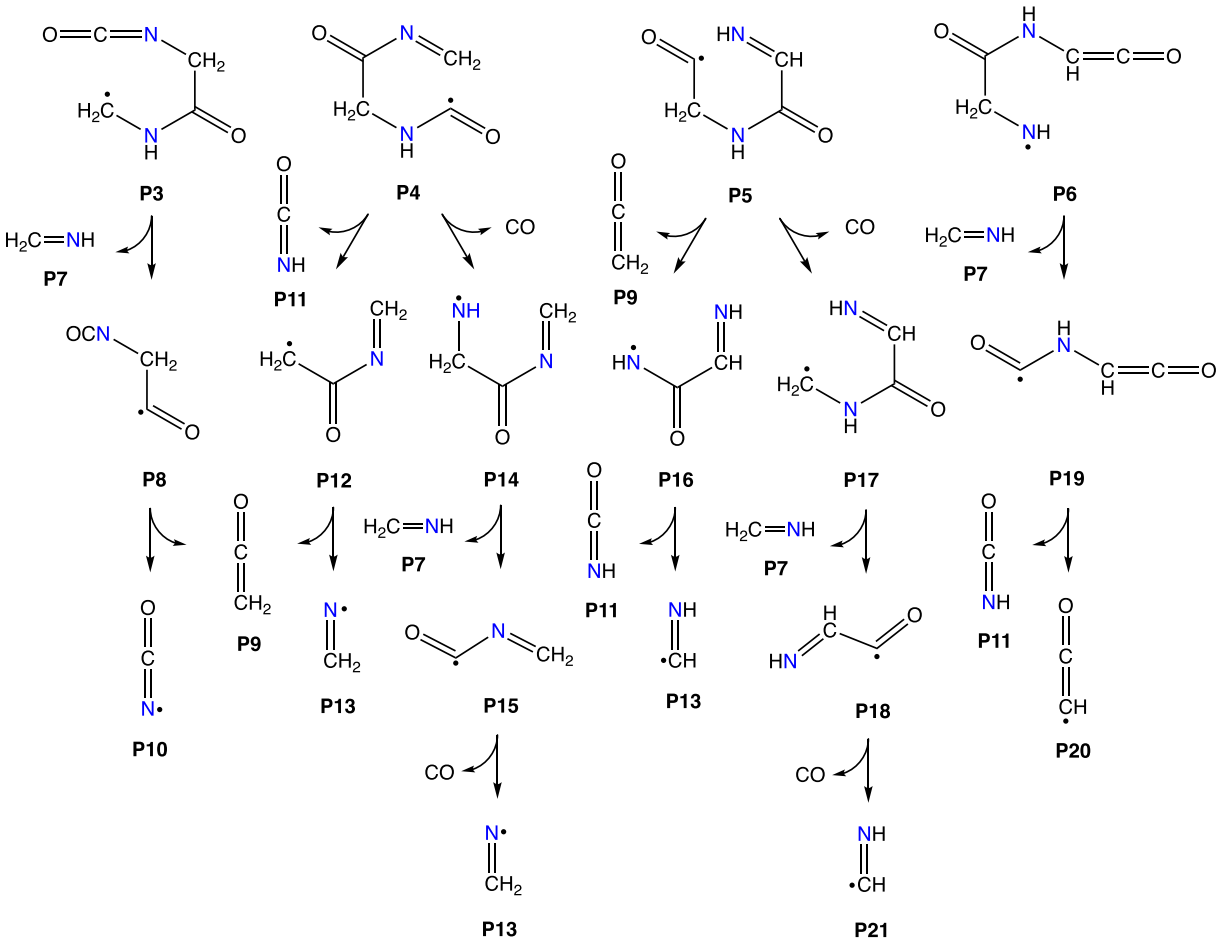

Fig. 4. Reaction network of the NO_X precursor release during the pyrolysis of 2,5-Diketopiperazine.

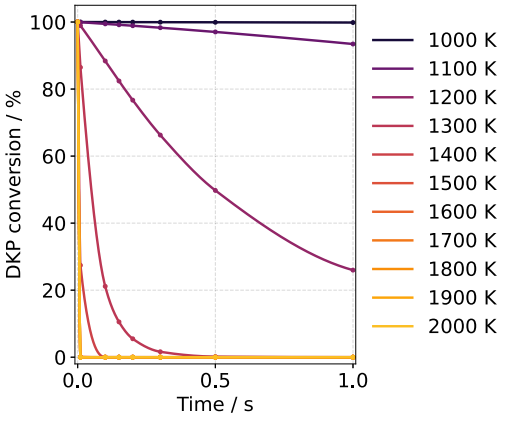

Fig. 5. DKP conversion (%) over time (0 – 1.0 s) in the batch reactor at different temperatures (1000 – 2000 K).

as main pyrolysis products CO, HCNO, HCN, and NH_3. In the simulations, we observed mostly H_2N radicals instead of NH_3. They started to form in minor quantities after 4 ns as decomposition products of imines and isocyanates. We observed that when the peptide bond of DKP is cleaved, the formation of imines (C = NH) was preferred over that of primary amines (R – NH_2). Primary amines, like glycine, have been reported to eliminate during pyrolysis amino radicals H_2N [74]. It is, thus, expected that NH_3 is formed from later-stage pyrolysis reactions of the NO_X precursors shown in Fig. 2(b).

3.2. Main decomposition pathways

The ReaxFF simulations indicate that the pyrolysis of DKP is initiated by the formation of peptide radicals (**P1** or **P2**) by formal abstraction of a hydrogen atom. It was observed that a small fraction of DKP reacts under C-H and N-H bond dissociation forming atomic hydrogen which leads to **P1** and **P2** (Fig. 3). Under realistic pyrolysis conditions, radicals such as methyl (H_3C), atomic hydrogen (H), aminyl (H_2N), and hydroxyl (HO) exist in the high-temperature reactor and can react with DKP molecules as well. The formation of these radicals is likely initiated by C–H and N–H bond dissociation during the early pyrolysis stages. Once formed, these radicals can increase the overall reactivity by abstracting hydrogen atoms from DKP (radical propagation), thereby promoting its decomposition. Furthermore, it was observed that DKP can also react by eliminating molecular hydrogen (H_2). The dehydrogenated DKP can then react again with atomic hydrogen to form **P1** or **P2**. The homolytic cleavage of the N-C and C-C bonds in DKP has not been observed in the ReaxFF simulations. The reaction energies for these have thus been manually examined and have been found to be higher (more endothermic) than the hydrogen abstraction reactions.

The 1-yl (**P1**) and 2-yl (**P2**) forms of DKP can react in ring-opening reactions, forming the acyclic compounds **P3–P6**. Among the initial dissociation reactions, the formation of the 2-yl form of DKP is thermodynamically favored (Table 1). The hydrogen atom abstraction by aminyl radicals, forming ammonia, appears to be effectively barrierless in both cases (**R1** and **R2**) on the DFT potential surface when including zero-point vibrational energies. Moreover, the pyrolysis can also be promoted by methyl radicals forming methane. Reaction **R3**, forming

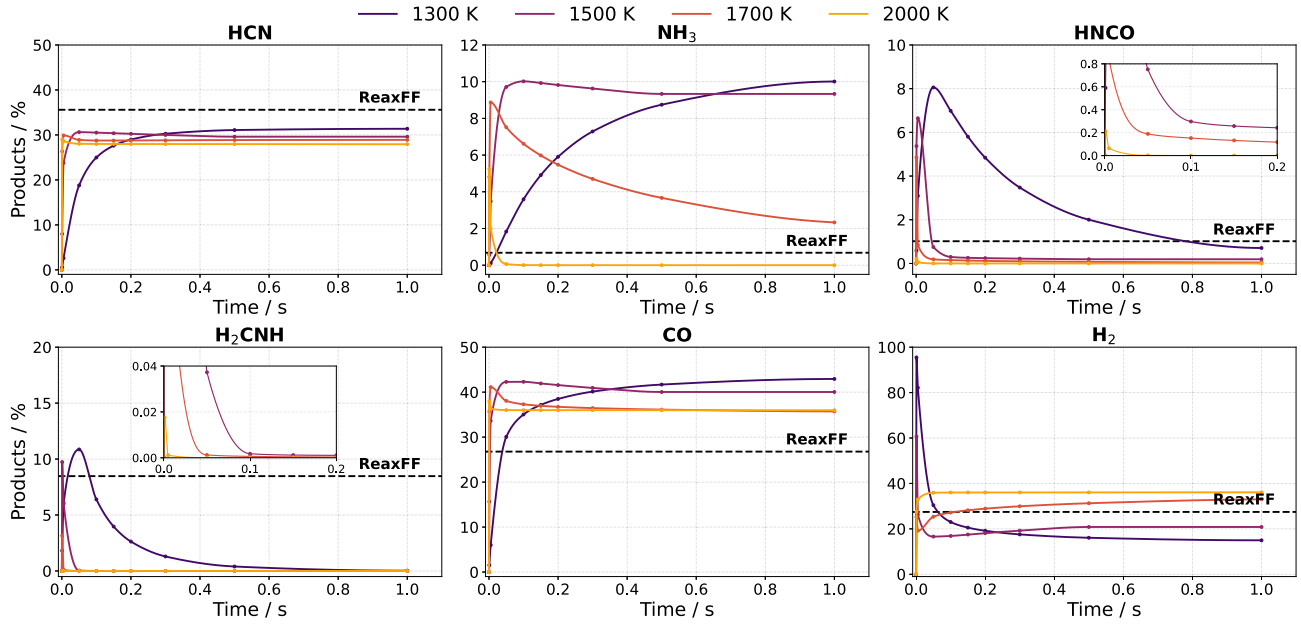

Fig. 6. Concentration profiles (mol%) of main pyrolysis products from isothermal and isochoric batch reactor simulations at varying temperatures. The dashed black line corresponds to ReaxFF predictions at 2000 K after 13.6 ns simulation time. Both simulations used the same initial concentrations for consistency ($\frac{1}{6}$ mol% DKP). (For interpretation of the references to colour in this figure legend, the reader is referred to the web version of this article.)

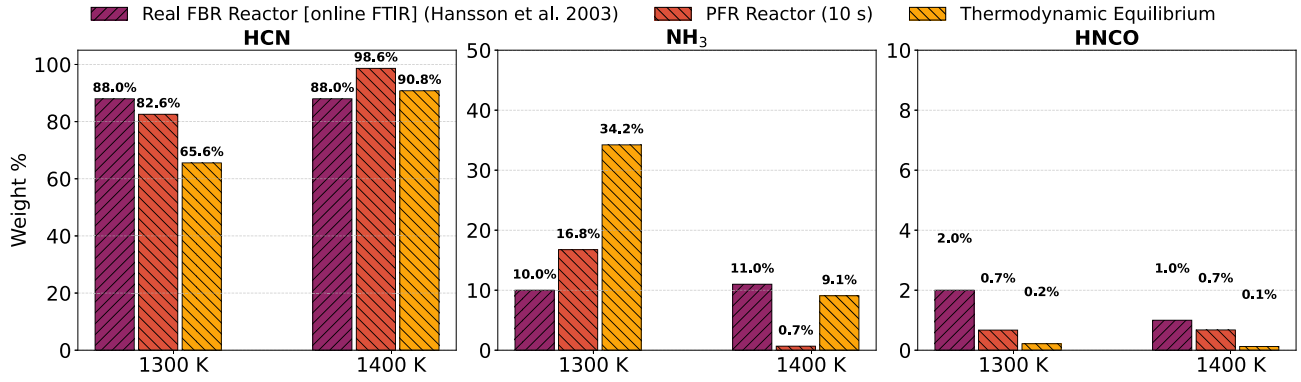

Fig. 7. Comparison of NO_X precursor formation from DKP pyrolysis in a real fluidized bed reactor (FBR) [15] and an ideal plug flow reactor (PFR) simulated with `OpenSMOKE++` under two conditions: short pyrolysis time ($\tau = 10$ s) and thermodynamic equilibrium. Reactor conditions: isothermal, isochoric, 1 mol% DKP in a N_2 atmosphere ($p = 1$ bar). Results are reported in wt.% normalized to the total weight of HCN, HNCO, NH_3, and NO.

species **P1**, requires an activation energy of 61.1 kJ/mol and is endothermic, while the H-abstraction leading to species **P2** releases −78.5 kJ/mol of energy with a barrier of 32.6 kJ/mol. Hydroxyl radicals react with DKP, forming water in addition to **P1** and **P2**. Reaction **R6** is highly exothermic releasing 138.0 kJ/mol of energy.

The ring opening of **P1** forming the intermediate **P3** requires an activation energy of 39.9 kJ/mol and releases an energy of −9.3 kJ/mol (Table 1). However, reactions **R14**–**R17** are endothermic reactions forming the compounds **P3**–**P6**, respectively. The ring opening of **P2** forming **P6** requires an energy of 225.4 kJ/mol while the formation of **P5** is less endothermic with an activation energy of 177.2 kJ/mol.

3.3. NO_X precursor release

The preferred decomposition channels of the reactive intermediates **P3**–**P6** are β-scissions. **P3** dissociates into methylene imine (**P7**) and the isocyanate **P8**. In the next step, the N-C bond breaks, yielding ethenone (**P9**) and an isocyanate radical (OCN). **P4** reacts either via β-scission to isocyanic acid (**P11**) and **P12** or via direct elimination of carbon monoxide (CO) to **P14**. The latter species eliminates barrierless methylene imine and via intermediate **P15** carbon monoxide and a methylene iminyl radical (**P13**). The elimination of carbon monoxide from **P15** is hindered by a barrier of 99.8 kJ/mol and with a reaction energy of 47.5 kJ/mol is endothermic (Table 2). Also for **P5** two alternative reaction pathways have been found. One reaction channel starts with the β-scission leading to ethenone and **P16**. An alternative pathway starts with the elimination of CO and formation of **P17**. The CO elimination pathway has a lower barrier of 35.0 kJ/mol compared to the release of **P9**. **P17** dissociates into methylene imine (**P7**) and the imino carbonyl **P18** which decomposes further into the iminyl radical **P21** and CO. The latter reaction has a barrier of 53.0 kJ/mol and a reaction energy of 26.3 kJ/mol. The energetically highest-lying ring-opening product **P6** dissociates into methylene imine and the ketene **P19** with a barrier of 90.5 kJ/mol. **P19** decomposes further into isocyanic acid and an open-shell ethenone species (**P20**) that can abstract hydrogen atoms from different species present in the reaction medium (Fig. 4).

3.4. Kinetic simulations

With the newly developed submodel for DKP, two types of kinetic simulations were performed with OpenSMOKE++:

a) pyrolysis in an isothermal batch reactor at different temperatures, and
b) a direct comparison of NO_X precursor formation in an ideal plug flow reactor (PFR) and experimental data from a real fluidized bed reactor (FBR).

3.4.1. Batch reactor simulations

Batch reactor simulations under isothermal and isochoric conditions were used to simulate pyrolysis times up to 1 s at temperatures between 1300 and 2000 K. The conversion of DKP in the ideal batch reactor, as shown in Fig. 5, depends strongly on the temperature. We note that the simulation does not yield full conversion of DKP below 1200 K. At 2000 K, the decomposition is nearly instantaneous, reaching complete conversion within just 1 ms. In contrast, at 1300 K, only about 75% of DKP is converted over the same time span. As expected, the conversion rate increases significantly with rising temperature.

Normalized concentrations (in mol%) of the formed N-containing intermediates and products (HCN, NH_3, HNCO, H_2CNH) as well as of CO and H_2 are compared in Fig. 6 as functions of pyrolysis time. The profiles of the main products indicate that the final concentration of hydrogen cyanide (HCN) is not significantly influenced by the pyrolysis temperature. After 0.2 seconds it reaches for all studied temperatures a nearly constant value of 28–30%. In contrast, ammonia (NH_3) is formed in significant amounts only at temperatures between 1300 and 1500 K with yields below 1% at 2000 K. Similarly, HNCO and methylene imine (H_2CNH) are, due to their thermal instability, only formed in notable amounts at around 1300 K. Also the formation of molecular hydrogen (H_2) is highly temperature-dependent. At 1300 K, the hydrogen concentration exceeds 90% after 1 ms, then declines to below 20% after 0.3 s. This peak in concentration is attributed to the incomplete conversion of DKP. The hydrogen concentration increases with pyrolysis temperature due to the increasing relevance of endothermic dehydrogenation reactions at higher temperatures that are largely driven by H-abstractions by atomic H from DKP and other species in the reaction medium. At lower temperatures the final H_2 concentrations are between 15 and 20%.

In comparison with the ideal batch reactor simulations performed with OpenSMOKE++, the concentration of HCN observed in the ReaxFF simulations is higher than that predicted at longer timescales in the kinetic model. This discrepancy is likely due to underestimated reaction barriers for HCN elimination or the limited simulation time of only 13.6 ns. While the batch reactor model predicts negligible ammonia formation at 2000 K, ReaxFF yields non-negligible concentrations, reaching nearly 1%. Atomistic simulations with ReaxFF rely on parameterized force fields, include only a limited number of atoms, and inherently neglect electronic structure and spin states. As a result, ReaxFF offers only qualitative insights into product formation. The simulation of systems containing several moles with timescales in the order of seconds is computationally infeasible. Nonetheless, the ReaxFF pyrolysis simulation captures qualitatively the formation of the main pyrolysis products, with only minor deviations from the results of the batch reactor simulations. This supports its potential use as a tool for reaction discovery.

3.4.2. Plug flow reactor

Hansson et al. performed DKP pyrolysis experiments in a fluidized bed reactor and reported results for the formation of NO_X precursors in weight percentages (wt.%) for different temperatures [15] with the total weight of formed HCN, HNCO, NH_3, and NO normalized to 100%. To compare with this experiment, we performed simulations with the plug flow reactor (PFR) implementation in OpenSMOKE++.

Both, in the experiments and the simulations no significant amount of nitrogen monoxide (NO) was detected, as expected for an oxygen-free environment. In the model predictions (PFR), the amount of hydrogen cyanide is slightly overestimated at 1400 K, likely due to the underestimation of ammonia. In the simulation, a larger fraction of ammonia is converted to HCN than in the experiment. A reason for this might be that in experiment, particularly at 1400 K, the reaction conditions have not been strictly within the kinetic regime, as indicated by the comparison with equilibrium calculations shown in Fig. 7 in orange color. In the experiment, the formation of NH_3 and HCN was almost insensitive to the temperature. In the simulations, the formation of ammonia is highly temperature dependent and more favored at lower temperatures (1300 K). HCNO is only formed in small amounts which is qualitatively captured by the simulation.

Fig. 8 shows the distribution of the main products in the plug flow reactor simulations as function of the temperature. HCN begins to form in significant amounts above 1100 K becoming nearly temperature-independent at higher temperatures as observed also above in the batch reaction simulations with shorter contact times (Fig. 8). Ammonia (NH_3) is formed in notable concentrations between 1100 and 1600 K, reaching a maximum of ≈ 10% around 1300 K. The formation of HNCO and methylene imine (H_2CNH) is highly temperature-dependent, as these species only form at lower temperatures (between 1000–1100 K) likely due to incomplete conversion. They become unstable at higher temperatures where they react further to NH_3, HCN, and CO. In cases of incomplete conversion, molecular hydrogen (H_2) forms in significant quantities, around 80% at 1000 K, reaching a minimum between 1000 and 1400 K. The formation behavior of H_2 and CO is mirror-symmetric; CO formation reaches its maximum precisely at the minimum of hydrogen formation.

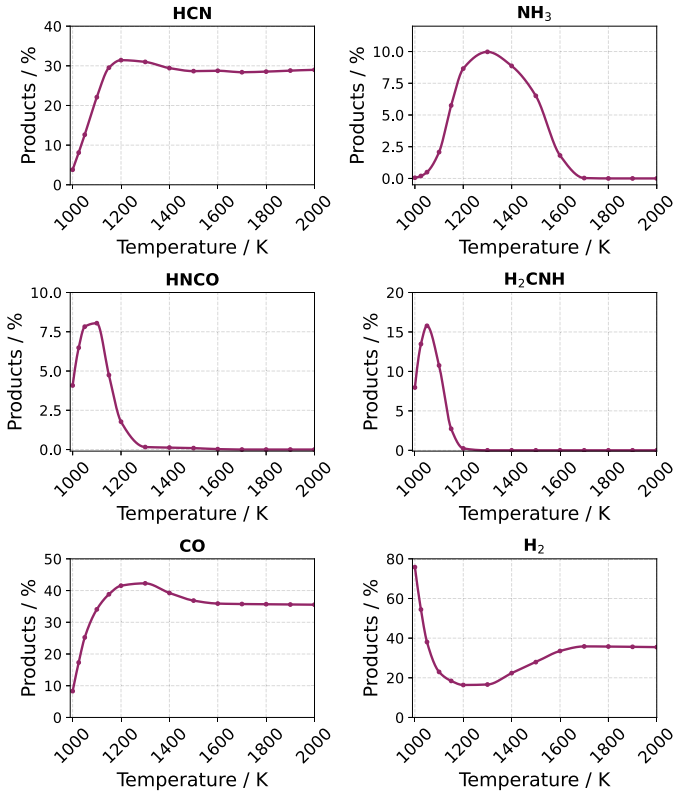

Fig. 8. Main pyrolysis products (mol%) as a function of temperature, simulated in an ideal plug flow reactor using OpenSMOKE++ for short–time pyrolysis (10 s) of DKP. Reactor conditions: isothermal, isochoric operation; 1 mol% DKP in a N_2 atmosphere (p = 1 bar).

4. Conclusions

This study presents the development of a kinetic submodel for the pyrolytic decomposition of 2,5-diketopiperazine, a representative cyclic peptide present in biomass. The focus of the model validation has been on the formation of NO_X precursors under oxygen-free conditions, given their relevance to environmental impact and biomass conversion processes. Model predictions were qualitatively compared with experimental data from Ref. [15] obtained in a fluidized bed reactor.

To discover possible decomposition pathways, ReaxFF MD simulations were performed, and key reactions were refined using an automated workflow that generated DFT-optimized geometries and coupled cluster reaction and activation energies. At 2000 K, DKP rapidly fragments into smaller intermediates, including methylene imine, isocyanic acid, and ethenone. This fragmentation begins with the formal abstraction of hydrogen atoms from C–H or N–H bonds. In later stages of pyrolysis, methyl, aminyl, and other gas-phase radicals are also formed, which can abstract hydrogen atoms from additional DKP molecules. The resulting DKP radicals subsequently undergo β-scission and decompose into smaller fragments such as NO_X precursors and carbon monoxide (CO).

The thermodynamic properties of DKP, its reaction intermediates, and products were fitted to `NASA-7` polynomials and incorporated into the `CRECK 2003 TOT HT LT SOOT NOX` mechanism using a `Python` subroutine. The kinetic parameters were fitted to a modified Arrhenius expression and similarly integrated into the mechanism. The resulting submodel was then implemented into the CRECK kinetic modeling framework. To validate the developed submodel, we carried out simulations with the `OpenSMOKE++` suite of ideal reactor solvers.

The main pyrolysis products of DKP predicted by the kinetic simulations are HCN, NH_3, CO, and H_2. HCN forms rapidly and its fraction in the product distribution is nearly temperature-independent between 1100 and 2000 K. In contrast, NH_3 is formed only at lower temperatures between 1300 and 1500 K and disappears above 1500 K. HNCO and H_2CNH are produced only at low temperatures due to their thermal instability. ReaxFF simulations qualitatively reproduce these trends but tend to overestimate HCN and NH_3 yields. Ideal plug flow reactor simulations show good qualitative agreement with measured NO_X yields in fluidized bed reactors. Differences in the results for NH_3 formation are attributed to differences in reaction regimes and complex fluid dynamics between the simulated reactor and the real reactor used for the measurements of the available experimental speciation data on DKP pyrolysis.

In conclusion, we developed the first kinetic submodel dedicated to DKP pyrolysis and showed that it provides consistent predictions of pyrolysis products over a wide range of temperatures. Electronic structure calculations of thermochemical kinetic parameters of the unraveled reaction pathways and compilation of detailed mechanistic kinetic mechanisms for reactor simulations using tools such as `OpenSMOKE++` remain the only practical approach for the prediction of product distributions and reactivity assessments at realistic operating conditions in the context of thermochemical conversion processes. It can serve as a foundation for further refinements and motivate experiments under well-defined reactor conditions tailored to the measurement of chemical kinetics for model development.

CRediT authorship contribution statement

Bastian Schnieder: Writing – original draft, Validation, Methodology, Investigation, Data curation, Conceptualization. **Paulo Debiagi:** Writing – original draft, Validation, Methodology, Conceptualization. **Matteo Pelucchi:** Writing – original draft, Validation, Supervision, Project administration, Methodology. **Rochus Schmid:** Writing – review & editing, Supervision, Project administration, Methodology, Funding acquisition. **Christof Hättig:** Writing – review & editing, Writing – original draft, Supervision, Project administration, Methodology, Funding acquisition.

Declaration of competing interest

The authors declare that they have no known competing financial interests or personal relationships that could have appeared to influence the work reported in this paper.

Acknowledgement

The authors thank the German Research Foundation (DFG) for funding this study within the framework of the SFB/Transregio 129 Oxyflame (Project number 215035359).

Appendix A

Table 3
Rate Constant Parameters for the Modified Arrhenius Expressions for the Pyrolysis of 2,5-Diketopiperazine.

Reaction	ln$A$	n	E/T	units of $k(T)$
P0 + H_2N → P1 + NH_3	barrierless			
P0 + H_2N → P2 + NH_3	barrierless			
P0 + H → P1 + H_2	15.51	2.0637	7709.45	cm^3/mol/s
reverse	9.42	2.4412	4921.57	cm^3/mol/s
P0 + H → P2 + H_2	barrierless			
P0 + H_3C → P1 + CH_4	6.13	2.4864	5928.63	cm^3/mol/s
reverse	6.28	2.5292	3990.86	cm^3/mol/s
P0 + H_3C → P2 + CH_4	6.79	2.3983	2601.57	cm^3/mol/s
reverse	7.37	2.3968	12,204.63	cm^3/mol/s
P1 → P3	27.78	0.3771	5062.12	1/s
reverse	21.24	0.6956	5475.36	1/s
P1 → P4	31.00	0.1440	11,158.81	1/s
reverse	22.31	0.7915	3724.81	1/s
P2 → P5	29.26	0.3122	21,691.90	1/s
reverse	21.55	0.8725	3142.55	1/s
P2 → P6	barrierless			
P3 → P7 + P8	32.93	-0.1828	17,502.53	1/s
reverse	3.30	2.5784	1149.81	cm^3/mol/s
P8 → P9 + P10	barrierless			
P4 → P11 + P12	27.93	0.4545	9999.34	1/s
reverse	9.29	1.8015	8201.12	cm^3/mol/s
P12 → P9 + P13	29.39	0.3972	15,621.19	1/s
reverse	4.56	2.6318	4836.61	cm^3/mol/s
P4 → P14 + CO	31.54	0.0660	11,432.82	1/s
reverse	14.21	1.4428	2641.78	cm^3/mol/s
P14 → P7 + P15	barrierless			
P15 → P13 + CO	31.14	-0.0139	12,191.18	1/s
reverse	10.52	2.1051	5493.26	cm^3/mol/s
P5 → P9 + P16	barrierless			
P16 → P11 + P21	30.44	0.2632	7673.50	1/s
reverse	5.91	2.5729	6740.03	cm^3/mol/s
P5 → P17 + CO	31.61	0.0213	4616.55	1/s
reverse	17.15	1.0462	3572.45	cm^3/mol/s
P17 → P7 + P18	barrierless			
P18 → P13 + CO	30.72	0.4152	7051.13	1/s
reverse	13.99	1.9239	2716.47	cm^3/mol/s
P6 → P7 + P19	32.33	-0.0825	11,345.38	1/s
reverse	7.59	2.1191	2002.08	cm^3/mol/s
P19 → P7 + P11	30.33	0.3081	9847.37	1/s
reverse	7.22	2.7501	5086.37	cm^3/mol/s
P0 → P22 + H_2	23.01	1.2275	38,172.45	1/s
reverse	11.04	2.1928	18,651.27	cm^3/mol/s

Appendix B. Supplementary data

Supplementary data for this article can be found online at doi:10.1016/j.fuel.2026.138472.

Data availability

The DFT-optimized geometries along with the electronic energies of the reactants, products, and transition states of the studied reactions, as well as the generated `NASA-7` polynomials are available in a Zenodo repository [75] or upon request from the authors.

References

[1] Matek B, Gawell K. The benefits of baseload renewables: a misunderstood energy technology. Electr J 2015;28(2):101–12. https://doi.org/10.1016/j.tej.2015.02.001

[2] Yang X, Zhao Z, Zhao Y, Xu L, Feng S, Wang Z, Zhang L, Shen B. Effects of torrefaction pretreatment on fuel quality and combustion characteristics of biomass: a review. Fuel 2024;358:130314. https://doi.org/10.1016/j.fuel.2023.130314

[3] Cheng J. Biomass to renewable energy processes. CRC Press; 2017.

[4] Neves D, Thunman H, Matos A, Tarelho L, Gómez-Barea A. Characterization and prediction of biomass pyrolysis products. Prog Energy Combust Sci 2011;37(5):611–30. https://doi.org/10.1016/j.pecs.2011.01.001

[5] Al-Rumaihi A, Shahbaz M, Mckay G, Mackey H, Al-Ansari T. A review of pyrolysis technologies and feedstock: a blending approach for plastic and biomass towards optimum biochar yield. Renew Sustain Energy Rev 2022;167:112715. https://doi.org/10.1016/j.rser.2022.112715

[6] Palla S, Surya DV, Pritam K, Puppala H, Basak T, Palla VCS. A critical review on the influence of operating parameters and feedstock characteristics on microwave pyrolysis of biomass. Environ Sci Pollut Res 2024;31(46):57570–93. https://doi.org/10.1007/s11356-024-33607-0

[7] Tian Y, Perré P. Effects of particle size on the pyrolysis of spruce and poplar: thermogravimetric analyses, DAEM modelling, validation, and prediction of secondary charring. Biomass and Bioenergy 2023;176:106913. https://doi.org/10.1016/j.biombioe.2023.106913

[8] Papa AA, Bartolucci L, Cordiner S, Di Carlo A, Mele P, Mulone V, Vitale A. The effect of pyrolysis temperature on the optimal conversion of residual biomass to clean syngas through fast-pyrolysis/steam gasification integration. Int J Hydrogen Energy 2024;95:1316–27. https://doi.org/10.1016/j.ijhydene.2024.09.100

[9] Ranzi E, Debiagi PEA, Frassoldati A. Mathematical modeling of fast biomass pyrolysis and bio-oil formation. Note i: kinetic mechanism of biomass pyrolysis. ACS Sustain Chem Eng 2017;5(4):2867–81. https://doi.org/10.1021/acssuschemeng.6b03096

[10] Ren Q, Zhao C. NO_x and n_2o precursors from biomass pyrolysis: role of cellulose, hemicellulose and lignin. Environ Sci Technol 2013;47(15):8955–61. https://doi.org/10.1021/es4017574

[11] Tian F-J, Li B-Q, Chen Y, Li C-Z. Formation of NO_x precursors during the pyrolysis of coal and biomass. Part v. Pyrolysis of a sewage sludge. Fuel 2002;81(17):2203–8.

[12] Zhuang X, Song Y, Wang X, Zhan H, Yin X, Wu C, Wang P. Pyrolysis of hydrothermally pretreated biowastes: the controllability on the formation of NO_x precursors. Chem Eng J 2020;393:124727.

[13] Zhan H, Zhuang X, Song Y, Yin X, Cao J, Shen Z, Wu C. Step pyrolysis of n-rich industrial biowastes: regulatory mechanism of NO_x precursor formation via exploring decisive reaction pathways. Chem Eng J 2018;344:320–31. https://doi.org/10.1016/j.cej.2018.03.099

[14] Chen H, Shan R, Zhao F, Gu J, Zhang Y, Yuan H, Chen Y. A review on the NOx precursors release during biomass pyrolysis. Chem Eng J 2023;451:138979. https://doi.org/10.1016/j.cej.2022.138979

[15] Hansson K-M, Samuelsson J, Tullin C, Åmand L-E. Formation of HNCO, HCN, and NH_3 from the pyrolysis of bark and nitrogen-containing model compounds. Combustion and Flame 2004;137(3):265–77. https://doi.org/10.1016/j.combustflame.2004.01.005

[16] Leng L, Yang L, Zu H, Yang J, Ai Z, Zhang W, Peng H, Zhan H, Li H, Zhong Q. Insights into glycine pyrolysis mechanisms: integrated experimental and molecular dynamics/DFT simulation studies. Fuel 2023;351:128949. https://doi.org/10.1016/j.fuel.2023.128949

[17] Liu J, Zhao W, wei Yang S, Hu B, xin Xu M, Ma S-W, Lu Q. Formation mechanism of NOx precursors during the pyrolysis of 2, 5-diketopiperazine based on experimental and theoretical study. Sci Total Environ 2021;801:149663. https://doi.org/10.1016/j.scitotenv.2021.149663

[18] Zhan H, Zhang X, Yin X, Wu C. Formation of nitrogenous pollutants during biomass thermo-chemical conversion. Prog Chem 2016;28(12):1880.

[19] Aydın H, İlkılıç C. AIR pollution, pollutant emissions and harmfull effects. J Eng Technol 2017;1(1):8–15.

[20] Zhang R, Tie X, Bond DW. Impacts of anthropogenic and natural NO_x sources over the US on tropospheric Chemistry. Proc Natl Acad Sci 2003;100(4):1505–9.

[21] Singh A, Agrawal M. Acid rain and its ecological consequences. J Environ Biol 2007;29(1):15.

[22] Li Y, Sarathy SM. Probing hydrogen–nitrogen chemistry: a theoretical study of important reactions in n_xh_y, HCN and HNCO oxidation. Int J Hydrogen Energy 2020;45(43):23624–37. https://doi.org/10.1016/j.ijhydene.2020.06.083

[23] Dagaut P, Lecomte F, Chevailler S, Cathonnet M. The oxidation of HCN and reactions with nitric oxide: experimental and detailed kinetic modeling. Combust Sci Technol 2000;155(1):105–27. https://doi.org/10.1080/00102200008947286

[24] Glarborg P, Jensen AD, Johnsson JE. Fuel nitrogen conversion in solid fuel fired systems. Prog Energy Combust Sci 2003;29(2):89–113. https://doi.org/10.1016/S0360-1285(02)00031-X

[25] Debiagi PEA, Gentile G, Pelucchi M, Frassoldati A, Cuoci A, Faravelli T, Ranzi E. Detailed kinetic mechanism of gas-phase reactions of volatiles released from biomass pyrolysis. Biomass and Bioenergy 2016;93:60–71.

[26] Pelucchi M, Arunthanayothin S, Song Y, Herbinet O, Stagni A, Carstensen H-H, Faravelli T, Battin-Leclerc F. Pyrolysis and combustion Chemistry of pyrrole, a reference component for bio-oil surrogates: jet-stirred reactor experiments and kinetic modeling. Energy Fuels 2021;35(9):7265–84.

[27] Chen B, Liu P, Pelucchi M, Guidici C, Maffei LP, Faller S, Xu Q, Huang J, Zhang F, Huang C, et al. New insights into the oxidation Chemistry of pyrrole, an n-containing biomass tar component. Proc Combust Inst 2023;39(1):73–84.

[28] Stagni A, Cavallotti C, Arunthanayothin S, Song Y, Herbinet O, Battin-Leclerc F, Faravelli T. An experimental, theoretical and kinetic-modeling study of the gas-phase oxidation of ammonia. React Chem Eng 2020;5(4):696–711.

[29] Song Y, Marrodán L, Vin N, Herbinet O, Assaf E, Fittschen C, Stagni A, Faravelli T, Alzueta MU, Battin-Leclerc F. The sensitizing effects of no2 and no on methane low temperature oxidation in a jet stirred reactor. Proc Combust Inst 2019;37(1):667–75.

[30] Chen B, Faller S, Maffei LP, Nobili A, Pelucchi M, Lu X, Pitsch H. N-containing pollutant formation in pyrrole counterflow diffusion flames. Combustion and Flame 2025;276:114136.

[31] Dai G, Li X, Lin H, Zhang Y, Hu Z, Zhang J, Tan H, Wang X. Nitrogen migration of biomass nitrogen-containing model compound (2, 5-diketopiperazine) during pressurized pyrolysis/gasification: effect of pressure and atmosphere. Fuel 2024;376:132689. https://doi.org/10.1016/j.fuel.2024.132689

[32] CRECK Modeling. Creck modeling group; 2023. https://www.creckmodeling.polimi.it/kinetics-mechanisms/[accessed: 31 July 2025].

[33] CRECK Modeling Lab. Kinetic mechanism; 2025. https://github.com/CRECKMODELING[accessed: 31 July 2025].

[34] Yönder Ö, Schmitz G, Schmid R, Schnieder B, Hättig C. A computational Chemistry study on the evolution of oxygen functional groups during char burnout. Fuel 2024;365:131217. https://doi.org/10.1016/j.fuel.2024.131217

[35] Schnieder B, Schmid R, Hättig C. Quantum chemical study on the evolution of sulfur functional groups during char burnout. J Phys Chem A 2025;129(14):3300–14, pMID: 40146532. https://doi.org/10.1021/acs.jpca.4c07973

[36] van Duin ACT, Dasgupta S, Lorant F, Goddard WA. ReaxFF: a reactive force field for hydrocarbons. J Phys Chem A 2001;105(41):9396–409. https://doi.org/10.1021/jp004368u

[37] Chenoweth K, van Duin ACT, Goddard WA. ReaxFF reactive force field for molecular dynamics simulations of hydrocarbon oxidation. J Phys Chem A 2008;112(5):1040–53. https://doi.org/10.1021/jp709896w

[38] Schmitz G, Yönder O, Schnieder B, Schmid R, Hättig C. An automatized workflow from molecular dynamic simulation to quantum chemical methods to identify elementary reactions and compute reaction constants. J Comput Chem 2021;42(32):2264–82. https://doi.org/10.1002/jcc.26757

[39] Kee RJ, Rupley FM, Miller JA. Chemkin-II: a fortran chemical kinetics package for the analysis of gas-phase chemical kinetics, Tech. rep., Sandia National Lab. (SNL-CA), Livermore, CA (United States). Sep 1989. https://doi.org/10.2172/5681118. https://www.osti.gov/biblio/5681118

[40] Wood MA, van Duin ACT, Strachan A. Coupled thermal and electromagnetic induced decomposition in the molecular explosive αhmx; a reactive molecular dynamics study. J Phys Chem A 2014;118(5):885–95. https://doi.org/10.1021/jp406248m

[41] Thompson AP, Aktulga HM, Berger R, Bolintineanu DS, Brown WM, Crozier PS, Veld PJI', Kohlmeyer A, Moore SG, Nguyen TD, Shan R, Stevens MJ, Tranchida J, Trott C, Plimpton SJ. LAMMPS - a flexible simulation tool for particle-based materials modeling at the atomic, meso, and continuum scales. Comp Phys Comm 2022;271:108171. https://doi.org/10.1016/j.cpc.2021.108171

[42] Schmid R. Pylmps. 2025,. https://github.com/MOFplus/pylmps.git [accessed: 1 August 2025].

[43] Savitzky A, Golay MJE. Smoothing and differentiation of data by simplified least squares procedures. Anal Chem 1964;36(8):1627–39. https://doi.org/10.1021/ac60214a047

[44] Virtanen P, Gommers R, Oliphant TE, Haberland M, Reddy T, et al. SciPy 1.0: fundamental algorithms for scientific computing in Python. Nat Methods 2020;17:261–72. https://doi.org/10.1038/s41592-019-0686-2

[45] TURBOMOLE V7.6. A development of university of karlsruhe and forschungszentrum karlsruhe GmbH; 1989–2007 (2025, TURBOMOLE GmbH, since 2007; available from. http://www.turbomole.com [accessed: 7 January 2025].

[46] Eichkorn K, Treutler O, Öhm H, Häser M, Ahlrichs R. Auxiliary basis sets to approximate Coulomb potentials. Chem Phys Lett 1995;240(4):283–90. https://doi.org/10.1016/0009-2614(95)00621-A

[47] Eichkorn K, Weigend F, Treutler O, Ahlrichs R. Auxiliary basis sets for main row atoms and transition metals and their use to approximate Coulomb potentials. Theor Chem Acc 1997;97(1):119–24.

[48] Grimme S, Antony J, Ehrlich S, Krieg H. A consistent and accurate AB initio parametrization of density functional dispersion correction (DFT-d) for the 94 elements H-Pu. J Chem Phys 2010;132(15):154104. https://doi.org/10.1063/1.3382344

[49] Tao J, Perdew JP, Staroverov VN, Scuseria GE. Climbing the density functional ladder: nonempirical meta–generalized gradient approximation designed for molecules and solids. Phys Rev Lett 2003;91:146401. https://doi.org/10.1103/PhysRevLett.91.146401

[50] Schäfer A, Horn H, Ahlrichs R. Fully optimized contracted Gaussian basis sets for atoms li to kr. J Chem Phys 1992;97(4):2571–7. https://doi.org/10.1063/1.463096

[51] Staroverov VN, Scuseria GE, Tao J, Perdew JP. Comparative assessment of a new nonempirical density functional: molecules and hydrogen-bonded complexes. J Chem Phys 2003;119(23):12129–37. https://doi.org/10.1063/1.1626543

[52] Schäfer A, Huber C, Ahlrichs R. Fully optimized contracted Gaussian basis sets of triple zeta valence quality for atoms li to kr. J Chem Phys 1994;100(8):5829–35. https://doi.org/10.1063/1.467146

[53] Csonka GI, Ruzsinszky A, Perdew JP. Estimation, computation, and experimental correction of molecular Zero-Point vibrational energies. J Phys Chem A 2005;109(30):6779–89. https://doi.org/10.1021/jp0519464

[54] Hättig C, Tew DP, Köhn A. Communications: accurate and efficient approximations to explicitly correlated coupled-cluster singles and doubles, CCSD-f12. J Chem Phys 2010;132(23):231102. https://doi.org/10.1063/1.3442368
[55] Peterson KA, Adler TB, Werner H-J. Systematically convergent basis sets for explicitly correlated wavefunctions: the atoms h, he, b–ne, and al–ar. J Chem Phys 2008;128(8):084102. https://doi.org/10.1063/1.2831537
[56] Hättig C. Optimization of auxiliary basis sets for RI-mp2 and RI-cc2 calculations: core-valence and quintuple-ζ basis sets for h to AR and QZVPP basis sets for li to kr. Phys Chem Chem Phys 2005;7:59–66. https://doi.org/10.1039/B415208E
[57] Weigend F, Köhn A, Hättig C. Efficient use of the correlation consistent basis sets in resolution of the identity mp2 calculations. J Chem Phys 2002;116(8):3175–83. https://doi.org/10.1063/1.1445115
[58] Yousaf KE, Peterson KA. Optimized auxiliary basis sets for explicitly correlated methods. J Chem Phys 2008;129(18):184108. https://doi.org/10.1063/1.3009271
[59] Häser M, Ahlrichs R. Improvements on the direct SCF method. J Comput Chem 1989;10(1):104–11. https://doi.org/10.1002/jcc.540100111
[60] Halgren TA, Lipscomb WN. The synchronous-transit method for determining reaction pathways and locating molecular transition states. Chem Phys Lett 1977;49(2):225–32. https://doi.org/10.1016/0009-2614(77)80574-5
[61] Elber R, Karplus M. A method for determining reaction paths in large molecules: application to myoglobin. Chem Phys Lett 1987;139(5):375–80. https://doi.org/10.1016/0009-2614(87)80576-6
[62] Mills G, Jónsson H. Quantum and thermal effects in h_2 dissociative adsorption: evaluation of free energy barriers in multidimensional quantum systems. Phys Rev Lett 1994;72:1124–7. https://doi.org/10.1103/PhysRevLett.72.1124
[63] Helgaker T. Transition-state optimizations by trust-region image minimization. Chem Phys Lett 1991;182(5):503–10. https://doi.org/10.1016/0009-2614(91)90115-P
[64] Yönder O, Schmitz G, Hättig C, Schmid R, Debiagi P, Hasse C, Locaspi A, Faravelli T. Can small polyaromatics describe their larger counterparts for local reactions? A computational study on the H-Abstraction reaction by an H-Atom from polyaromatics. J Phys Chem A 2020;124(46):9626–37. https://doi.org/10.1021/acs.jpca.0c07133
[65] Grimme S. Supramolecular binding Thermodynamics by Dispersion-Corrected density functional theory. Chem Eur J 2012;18(32):9955–64. https://doi.org/10.1002/chem.201200497
[66] Yönder Ö, Hättig C. Density functional theory study of CO formation through reactions of polycyclic aromatic hydrocarbons with atomic oxygen ($o(^3p)$). Fuel 2019;241:851–60. https://doi.org/10.1016/j.fuel.2018.12.047.
[67] Shavitt I. A calculation of the rates of the ortho-para conversions and isotope exchanges in hydrogen. J Chem Phys 1959;31(5):1359–67. https://doi.org/10.1063/1.1730599
[68] Cuoci A, Frassoldati A, Faravelli T, Ranzi E. OpenSMOKE++: an object-oriented framework for the numerical modeling of reactive systems with detailed kinetic mechanisms. Comput Phys Commun 2015;192:237–64. https://doi.org/10.1016/j.cpc.2015.02.014
[69] Gordon S, McBride BJ. Computer program for calculation of complex chemical equilibrium compositions, rocket performance, incident and reflected shocks, and Chapman-Jouguet detonations. Interim revision, march 1976, Tech. rep., Glenn Research Center; 1976.
[70] Boichot R. JANAF-thermochemical-tables-to-NASA-glenn-coefficients-converter. 2021. https://github.com/Raphael-Boichot/JANAF-thermochemical-tables-to-NASA-Glenn-coefficients-converter. matlab codes to generate NASA Glenn Coefficients from JANAF thermochemical tables.
[71] Schnieder B, Hättig C, Schmid R. Janaf2nasa converter. Nov, 2025. https://doi.org/10.5281/zenodo.17710369
[72] Cuoci A, Frassoldati A, Faravelli T, Ranzi E. Numerical modeling of laminar flames with detailed kinetics based on the Operator-Splitting method. Energy Fuels 2013;27(12):7730–53. https://doi.org/10.1021/ef4016334
[73] Stagni A, Cuoci A, Frassoldati A, Faravelli T, Ranzi E. Lumping and reduction of detailed kinetic schemes: an effective coupling. Ind Eng Chem Res 2014;53(22):9004–16. https://doi.org/10.1021/ie403272f
[74] Zheng Z-H, Du Wang D, Zhao L, Yang J-Z, Wang Z-D, Wang C-P, Tian Z-Y. The nitrogen migration investigation during the pyrolysis and oxidation of c3 amines. Fuel 2025;398:135532. https://doi.org/10.1016/j.fuel.2025.135532
[75] Schnieder B, Hättig C, Schmid R. Raw data to “computational study on the pyrolysis of 2, 5-diketopiperazine: from electronic structure calculations to kinetic modeling. Jul, 2024. https://doi.org/10.5281/zenodo.12755107